NANO · MICRO small
www.small-journal.com

Bandgap Engineering in 2D Lateral Heterostructures of Transition Metal Dichalcogenides via Controlled Alloying

*Florence A. Nugera, Prasana K. Sahoo, Yan Xin, Sharad Ambardar, Dmitri V. Voronine, Un Jeong Kim, Yoojoong Han, Hyungbin Son, and Humberto R. Gutiérrez**

2D heterostructures made of transition metal dichalcogenides (TMD) have emerged as potential building blocks for new-generation 2D electronics due to their interesting physical properties at the interfaces. The bandgap, work function, and optical constants are composition dependent, and the spectrum of applications can be expanded by producing alloy-based heterostructures. Herein, the successful synthesis of monolayer and bilayer lateral heterostructures, based on ternary alloys of $MoS_{2(1-x)}Se_{2x}$–$WS_{2(1-x)}Se_{2x}$, is reported by modifying the ratio of the source precursors; the bandgaps of both materials in the heterostructure are continuously tuned in the entire range of chalcogen compositions. Raman and photoluminescence (PL) spatial maps show good intradomain composition homogeneity. Kelvin probe measurements in different heterostructures reveal composition-dependent band alignments, which can further be affected by unintentional electronic doping during the growth. The fabrication of sequential multijunction lateral heterostructures with three layers of thickness, composed of quaternary and ternary alloys, is also reported. These results greatly expand the available tools kit for optoelectronic applications in the 2D realm.

F. A. Nugera, H. R. Gutiérrez
Department of Physics
University of South Florida
Tampa, FL 33620, USA
E-mail: humberto3@usf.edu

P. K. Sahoo
Materials Science Centre
Indian Institute of Technology Kharagpur
Kharagpur 721302, India

Y. Xin
National High Magnetic Field Laboratory
Florida State University
Tallahassee, FL 32310, USA

S. Ambardar, D. V. Voronine
Department of Physics, and Department of Medical Engineering
University of South Florida
Tampa, FL 33620, USA

U. J. Kim
Imaging Device Laboratory
Samsung Advanced Institute of Technology
Suwon, Gyeonggi-do 16419, Republic of Korea

Y. Han, H. Son
School of Integrative Engineering
Chung-Ang University
Seoul 06974, Republic of Korea

The ORCID identification number(s) for the author(s) of this article can be found under https://doi.org/10.1002/smll.202106600.

DOI: 10.1002/smll.202106600

1. Introduction

In the last two decades, the scientific community has dedicated significant resources to unveil the fundamental science and applications of 2D-layered materials.[1–4] Particularly, the family of transition metal dichalcogenides (TMDs)[3,5] with semiconductor behavior (e.g., MoS_2, $MoSe_2$, WS_2, and WSe_2) has shown great potential for optoelectronics,[6] spintronics,[7] and valleytronics[8] applications. The integration of different 2D materials to form heterostructures, either laterally or vertically, allows us to exploit the unique properties of each material in a single building block.[9] In 2D lateral heterostructures (LHSs), distinct materials are linked through strong in-plane covalent bonds; while in vertical heterostructures (VHSs), the stacked 2D materials are connected mainly through weak interlayer van der Waals interactions. LHSs have been produced by different approaches, including edge epitaxy of different materials,[10–17] postgrowth local chemical modifications such as lithography[18] and laser-assisted chemical exchange in a controlled atmosphere.[19]

Heterojunctions based on binary TMD semiconductor compounds (e.g., MoS_2, $MoSe_2$, WS_2, and WSe_2) only allow a total of six possible combinations. The available tools kit of physical properties can be significantly expanded through ternary alloys where the electronic and optical properties are finely tuned by controlling the composition ratio between the elemental constituents.[20–25] 2D TMD ternary alloys are mainly obtained by mixing the transition metal atoms ($Mo_{(1-y)}W_ySe_2$ or $Mo_{(1-y)}W_yS_2$)[20–22] or by mixing the chalcogen atoms ($MoS_{2(1-x)}Se_{2x}$ or $WS_{2(1-x)}Se_{2x}$).[23,24] The ability to continuously tailor the electronic bandgap represents a great potential for designing devices operating in a wide range of spectra with enhanced electronic, optical, and catalytic properties.[26] The work function is also composition dependent and has a direct impact on the band alignment at the interface of LHSs.[27]

Although composition-graded 2D structures have previously been reported,[28–32] there are a few reports on alloy-based LHSs, where the composition of each domain is controlled and homogeneous.[17,27,33] Here we demonstrate the continuous tuning of the bandgap in each domain of monolayer (1L) LHSs composed of ternary alloys $MoS_{2(1-x)}Se_{2x}$–$WS_{2(1-x)}Se_{2x}$. Raman and photoluminescence (PL) mapping reveal homogeneous composition in each domain. Kelvin probe force microscopy (KPFM) studies

confirm the different band alignments at the heterojunctions. Additionally, we report the synthesis of alloy-based bilayer (2L) and trilayer (3L) LHSs. In the case of 3L-LHSs, a combination of quaternary ($Mo_{1-y}W_yS_{2(1-x)}Se_{2x}$) and ternary ($WS_{2(1-x)}Se_{2x}$) alloys was obtained. It is worth mentioning that this is the first demonstration of bandgap tuning in both domains for 1L-LHSs, and the first report on few-layered alloy-based LHSs.

2. Results and Discussion

The alloyed heterostructures were synthesized via a water-assisted CVD approach (**Figure 1**a), recently developed in our group.[16,17] This method allows the sequential growth of heterostructures without exchanging CVD reactors or the solid sources. As shown in Figure 1a, the solid precursors ($MoSe_2$ and WS_2) were placed in the same ceramic boat within the quartz tube reactor and kept at 1060 °C, while the substrates (285 nm SiO_2/Si) were kept downstream at a lower temperature region (700–800 °C). As previously reported,[16,17] the composition of the carrier gas determines the selective deposition of the individual domains with distinct transition metal atoms. Using N_2+H_2O as the carrier gas favors the growth of Mo-rich domain, while switching to Ar+H_2 favors the growth of W-rich domains (see schematics in Figure 1b); details of the procedure as well as the growth mechanism have been published elsewhere.[16,17]

For the ternary alloys we used a combination of $MoSe_2$ and WS_2 powder sources; by changing the mass ratio of these precursors, it is possible to systematically control the relative concentration of Se and S in the gas precursors, and hence the chalcogen composition (x) of the ternary alloys in each domain of the $MoS_{2(1-x)}Se_{2x}$–$WS_{2(1-x)}Se_{2x}$ heterostructures. The lateral size of each domain can be controlled by increasing or decreasing the time of their corresponding growth step. The different domains in the heterostructures present a clear optical contrast (Figure 1c) as well as electronic contrast (Figure 1e). The low-magnification optical image in Figure 1d shows the abundance of 2D heterostructure islands on the substrate surface, as well as the coexistence of islands with different thicknesses in the same sample.

2.1. Bandgap Engineering in LHSs

The composition-dependent optical properties of the alloy-based lateral heterostructures were studied by PL and Raman spectroscopies. **Figure 2**a shows the PL spectra for 1L-LHSs from seven samples grown using different amounts of WS_2 and $MoSe_2$ in the powder sources. The peak positions of LHSs based on binary compounds ($x = 0$ and $x = 1$) are also included for reference. From left to right, the PL was taken at different points in the heterostructures, i.e., at the Mo-rich domain

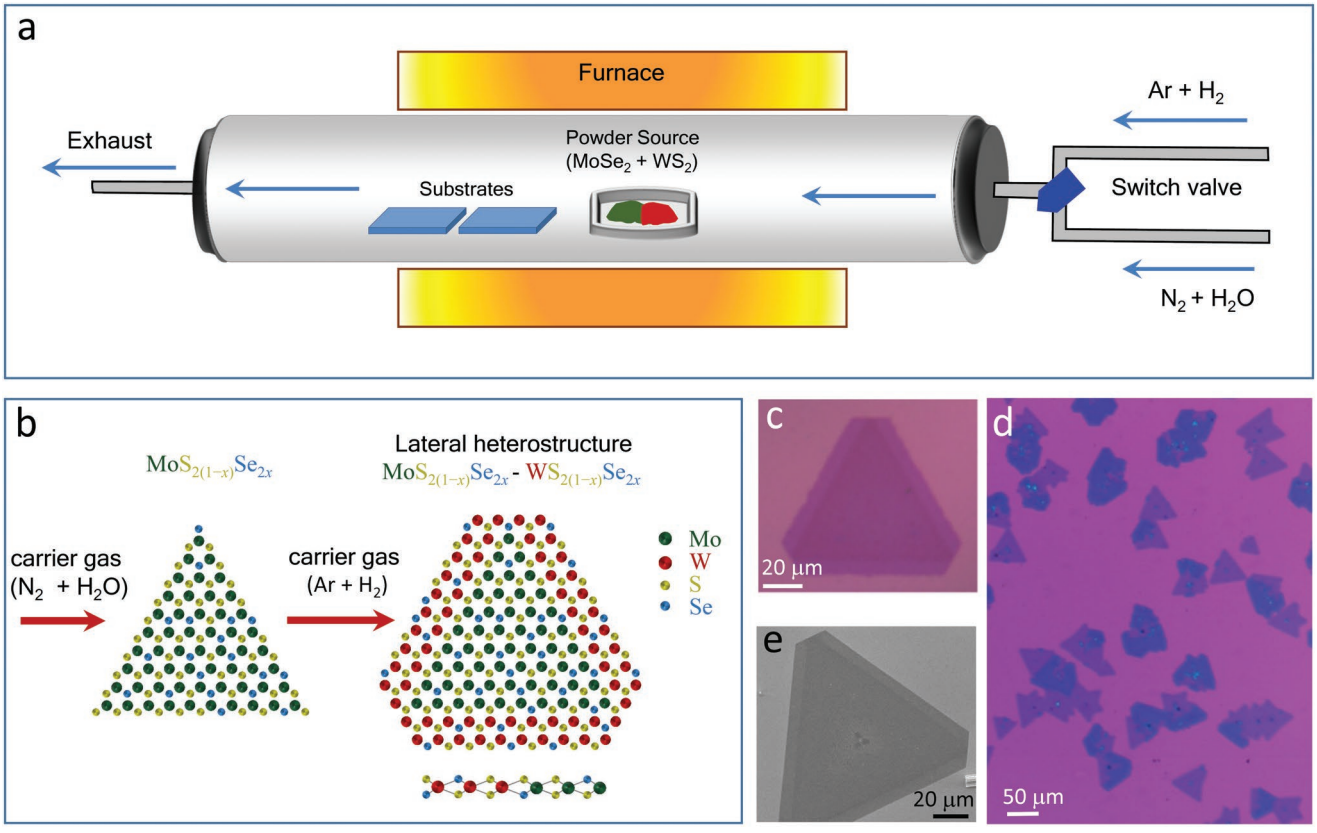

Figure 1. a) Schematics of the CVD growth process. b) Cartoons showing the atomic structure of the lateral heterostructures based on ternary alloys of $MoS_{2(1-x)}Se_{2x}$–$WS_{2(1-x)}Se_{2x}$. c,d) High- and low-magnification optical images of the as-grown heterostructures, respectively. e) Scanning electron microscopy (SEM) image of a lateral alloy heterostructure.

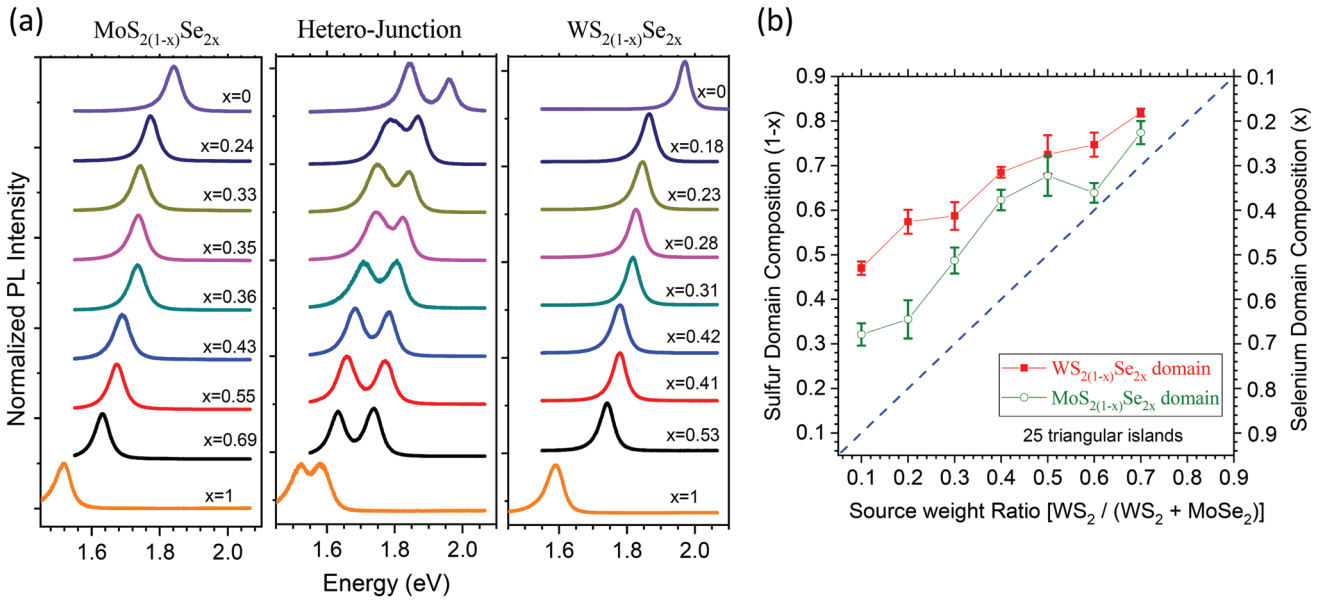

Figure 2. Continuous bandgap tuning in 1L-LHSs. a) PL spectra of seven different samples grown from powder sources with different compositions. The spectra on the left, center, and right panels were collected from the Mo-rich junction, and W-rich domain, respectively. b) Correlation between the average composition in the Mo-rich and W-rich domains versus the WS_2 content in the powder source (WS_2:$MoSe_2$).

(left panel), at the heterojunction (central panel), and at the W-rich domain (right panel). The chalcogen concentration (x) at each domain was calculated from the measured photoluminescence peak positions, according to the Vegard's law for ternary alloys: E_g ($MS_{2(1-x)}Se_{2x}$) = $(1 - x)E_g$ (MS_2) + xE_g (MSe_2) − bx $(1 - x)$); where M = [Mo or W], and considering bandgap bowing parameters $b = 0.05$ and $b = 0.04$ for the Mo-based and W-based alloys, respectively.[34]

It is evident in Figure 2a that the PL peaks for the two domains in the heterostructures consistently blueshift as the percentage of WS_2 relative to $MoSe_2$ increases in the source. This blueshift suggests a decrease in the selenium content ($2x$) at each domain due to the higher abundance of sulfur species in the carrier gas during the growth. The PL position, and hence the bandgap, was continuously tuned between 1.63 and 1.77 eV in the $MoS_{2(1-x)}Se_{2x}$ domain, and from 1.74 to 1.87 eV in the $WS_{2(1-x)}Se_{2x}$ domain. At the interface (central panel in Figure 2a), there is a superposition of two PL peaks due to the simultaneously excitation of the PL from both domains by the ≈0.4 µm laser spot. Our previous report on LHSs of binary WS_2–MoS_2 and WSe_2–$MoSe_2$ has shown that broad heterojunctions display a single PL peak at an intermediate energy that shifts with position due to a compositional gradient or alloying of the metallic element at the interface; this results in a smooth interface.[17] In contrast, for relatively sharp interfaces, its local PL displays two separated peaks corresponding to each individual domain.[17] The last scenario is the one observed in all the interfaces in Figure 2a. Even for sharp interfaces, we do not rule out a small alloying in the metal element for a region close to the interface, as we previously observed in binary LHSs. In Figure 2b, the composition (x) in each domain of the heterostructure is plotted as a function of the weight ratio of the source (WS_2/(WS_2 + $MoSe_2$)). Here, each point corresponds to the average composition of a specific domain calculated for 25 different islands in each sample, and the error bars in Figure 2b correspond to the standard deviation. The trends observed in Figure 2b for both domains are very similar, with a slightly higher sulfur content in the tungsten domains as compared to the molybdenum domains. The blue dashed line represents the ideal case scenario in which the composition of the source is stoichiometrically transferred to the sample. In general, the samples have a higher sulfur content compared to the source; this could be the result of higher abundance of sulfur species in the carrier gas due to differences in volatility between sulfur and selenium.

Next, we investigate in detail the PL and Raman spectra for two different monolayer-based heterostructures with distinct chalcogen contents. The first case, shown in **Figure 3**, consists of a 1L-LHS with a composition of $MoS_{1.32}Se_{0.68}$–$WS_{1.53}Se_{0.47}$ (high sulfur content). The optical image (Figure 3a) shows a clear contrast between the Mo-rich (darker contrast) and the W-rich (lighter contrast) domains. In this case, the growth times of the Mo-rich domain and W-rich domain were 12 and 3 min, respectively. The resultant average size of the islands was around 60 µm, while the lateral size of the W-rich domain, perpendicular to the interface, was ≈6 µm.

PL intensity maps (Figure 3b,c) from the area enclosed in the white dashed rectangle in Figure 3a show the spatially localized PL emission of each domain. The map corresponding to the PL peak position (Figure 3d) suggests a relatively good composition homogeneity of each domain forming the heterostructure. The PL spectra (Figure 3e) show strong excitonic peaks at around 1.84 eV for the W-rich domain (point 1) and 1.74 eV for the Mo-rich domain (point 2), which are at energies between those obtained for the binary counterparts. The domains' composition was calculated using the above PL peak position values. It is worth noticing, however, that there is a small band in the outer region on the Mo domain (color cyan in Figure 3d)

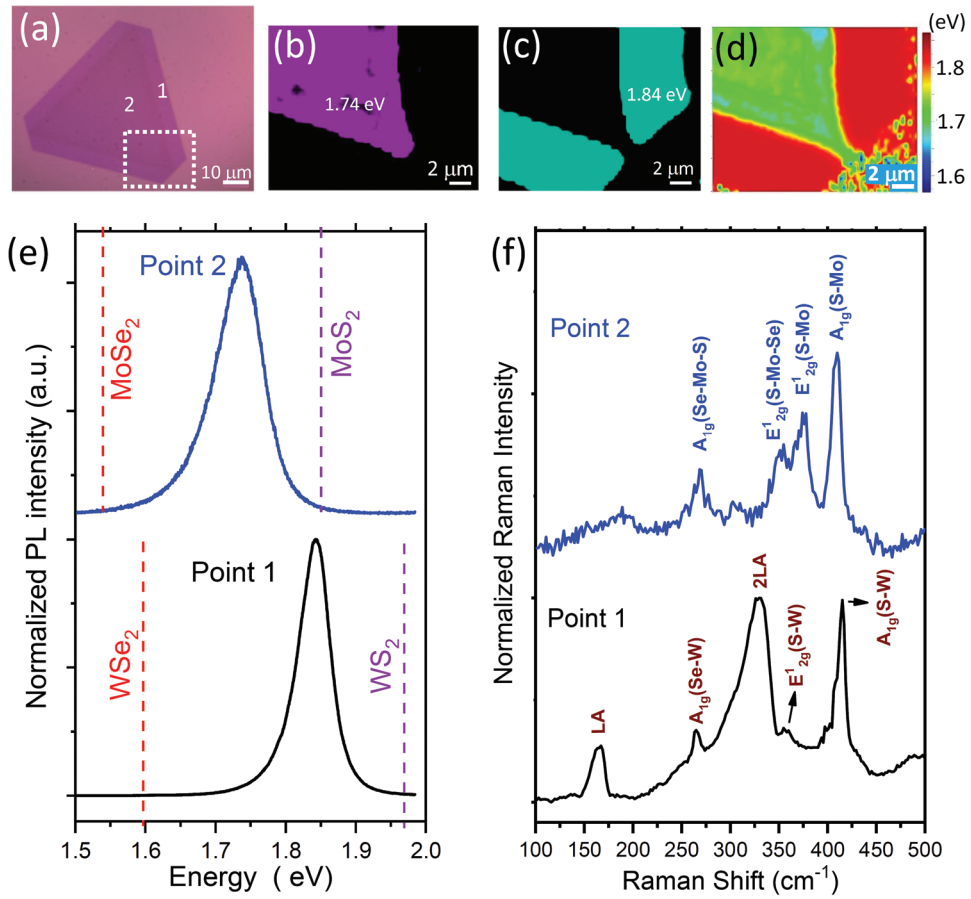

Figure 3. Monolayer (1L) lateral heterostructure, $MoS_{1.32}Se_{0.68}$–$WS_{1.53}Se_{0.47}$. a) Optical image of the LHS. b,c) Intensity PL maps for 1.74 and 1.84 eV, respectively, from the region within the dashed rectangle in panel (a). d) PL peak position map. e,f) PL and Raman spectra, respectively, at point 1 (W-rich domain) and point 2 (Mo-rich domain) as indicated in panel (a).

that presents a redshift in the PL peak position. Since just after this narrow region, the PL in the Mo domain returns to 1.74 eV before the growth is switched to the W domain, we believe that this redshift could be due to a localized fluctuation in the chalcogen ratio of the gas precursors.

The formation of $MoSe_{2(1-x)}S_{2x}$ and $WSe_{2(1-x)}S_{2x}$ alloys was also verified by Raman spectroscopy (Figure 3f). The Raman spectrum for the Mo-rich domain (top blue spectrum) shows the in-plane and out-of-plane MoS_2-like phonon modes at 376 cm^{-1} (E^1_{2g} (S—Mo)) and 409 cm^{-1} (A_{1g} (S—Mo)), respectively.[23,35,36] The peak around 270 cm^{-1} is an A_{1g} phonon mode with both Se and S atoms around the Mo atom (Se—Mo—S).[36] The peak at 351 cm^{-1} is also a composition-dependent E^1_{2g} impurity mode (Se—Mo—S).[36] As expected, for this composition (sulfur-rich), the $MoSe_2$-like Raman peaks (Se—Mo—S) are weaker compared to those related to MoS_2-like (S—Mo) modes. The Raman spectra of the W-rich domain (bottom black spectrum) show three optical phonon modes at 265 cm^{-1} (A_{1g} (Se—W)), 358 cm^{-1} (E^1_{2g} (S—W)), and 415 cm^{-1} (A_{1g} (S—W)).[24] Two additional peaks appear at 165 and 330 cm^{-1}, which we tentatively assign to the longitudinal acoustic (LA) and its second order replica 2LA, respectively. The rationale for this assignment is the high intensity of the 2LA peak,[37] and the fact that both (LA and 2LA) present similar phonon lineshapes. It is well known that, for a pure WS_2 monolayer, the most intense Raman peak corresponds to the 2LA mode (352 cm^{-1}) when using 514 and 532 nm excitation lasers; this is due to a double resonance in this second-order Raman scattering process.[37,38] Since this alloy has a high sulfur content, the second-order Raman process associated with the 2LA peak could still be close to a resonant condition, which explains its high intensity compared to other peaks. Notice that the LA and 2LA peaks for the alloy (165 and 330 cm^{-1}) are redshifted compared to pure WS_2 (176 and 352 cm^{-1}).[37] A Raman line scan across the domains (Figure S1a–c, Supporting Information) shows that the relative intensity and position of the Raman peaks in each domain remain constant. The assumption that each domain of the heterostructure is composed of ternary alloys was also verified by atomic resolution scanning transmission electron microscopy (STEM; Figure S2, Supporting Information) and energy dispersive spectroscopy (EDS) elemental analysis (Figure S3, Supporting Information).

The PL and Raman responses for a 1L-LHS with higher selenium concentration ($MoS_{0.48}Se_{1.52}$–$WS_{0.86}Se_{1.14}$) are shown in **Figure 4**. In this case, the optical image (Figure 4a) also shows a clear contrast between the Mo-rich (darker contrast) and the W-rich (lighter contrast) domains. The PL intensity maps obtained for 1.63 eV (Mo-rich domain) and 1.73 eV (W-rich domain) reveal the spatial distribution of the laterally

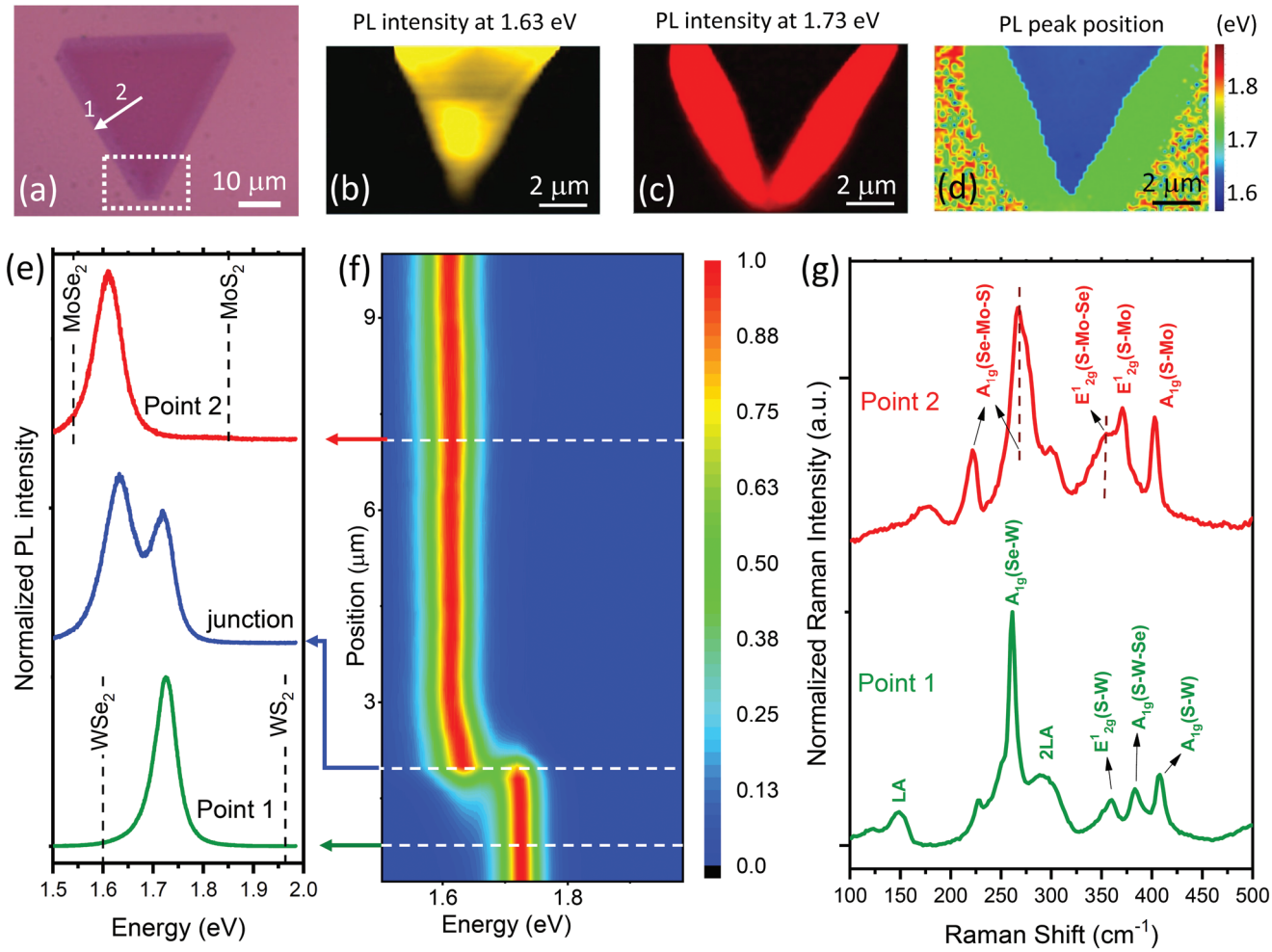

Figure 4. Monolayer (1L) lateral heterostructure $MoS_{0.48}Se_{1.52}$–$WS_{0.86}Se_{1.14}$. a) Optical image of the LHS. b,c) Intensity PL maps for 1.63 and 1.73 eV, respectively, from the region within the dashed rectangle in panel (a). d) PL peak position map. e,f) PL spectra at different positions and PL contour plot along the white arrow in panel (a). g) Raman spectra at points 1 and 2 in panel (a).

connected domains (Figure 4b,c). The PL peak position map (Figure 4d) also accounts for the intradomain compositional homogeneity. The PL spectra collected at points 1 and 2 (Figure 4e) present strong excitonic peaks at 1.73 and 1.63 eV, respectively. Figure 4f shows the PL color contour plot for a line scan along the arrow in Figure 4a; the position of the PL peak is nearly constant on each domain, suggesting a homogeneous distribution of the chalcogen ratio. However, close to the interface, in the molybdenum side, there is a small blueshift of 0.02 eV, suggesting a small variation of the composition in that vicinity. Just at the interface, two well-defined peaks are observed due to the simultaneous excitation of the two domains by the laser spot (Figure 4e). In general, an intensity variation of the PL signal can be noticed in the Mo domains of both monolayer heterostructures (see Figures 3b and 4b). Although the origin of the darker regions has not been determined at this point, a possible explanation could be fluctuations in the distribution of crystalline defects at the Mo domain. Higher density of defects can create nonradiative relaxation pathways for the photogenerated carriers that reduce the PL intensity.

The Raman spectra at point 2 (top red data in Figure 4g) correspond to the $MoS_{0.48}Se_{1.52}$ domain. A previous study[36] using polarized Raman spectroscopy has reported that, for this type of alloy with high selenium content, the $MoSe_2$ A_{1g} peak splits into two peaks, which further separate as the selenium (sulfur) content decreases (increases).[23,36] The two peaks are called $MoSe_2$-like A_{1g} phonon modes and correspond to different Se/S configurations around the Mo atom.[33] The Raman spectrum at the top of Figure 4g presents these two $MoSe_2$-like A_{1g} (Se−Mo−S) peaks at 222 and 267 cm^{-1}; additionally, a shoulder at 353 cm^{-1} is also related to a hybrid mode E^1_{2g} (Se−Mo−S). The MoS_2-like modes appear at 370 cm^{-1} (E^1_{2g} (S−Mo)) and 403 cm^{-1} (A_{1g} (S−Mo)). The $WS_{0.86}Se_{1.14}$ domain (bottom green spectrum in Figure 4g) presents the A_{1g} (S−W) at 408 cm^{-1} and the A_{1g} (Se−W) at 261 cm^{-1}, which are redshifted with respect to the sulfur-rich alloy in Figure 3f. The peak around 383 cm^{-1} has been previously observed for high selenium content and labeled as an A_{1g} (S−W−Se) mode,[24] which corresponds to a different Se/S configuration around the W atom. The E^1_{2g} (S−W) mode is at 358 cm^{-1}, and the LA and 2LA modes redshifted to 147 and 294 cm^{-1}, respectively. Notice that, the $MoSe_2$-like and

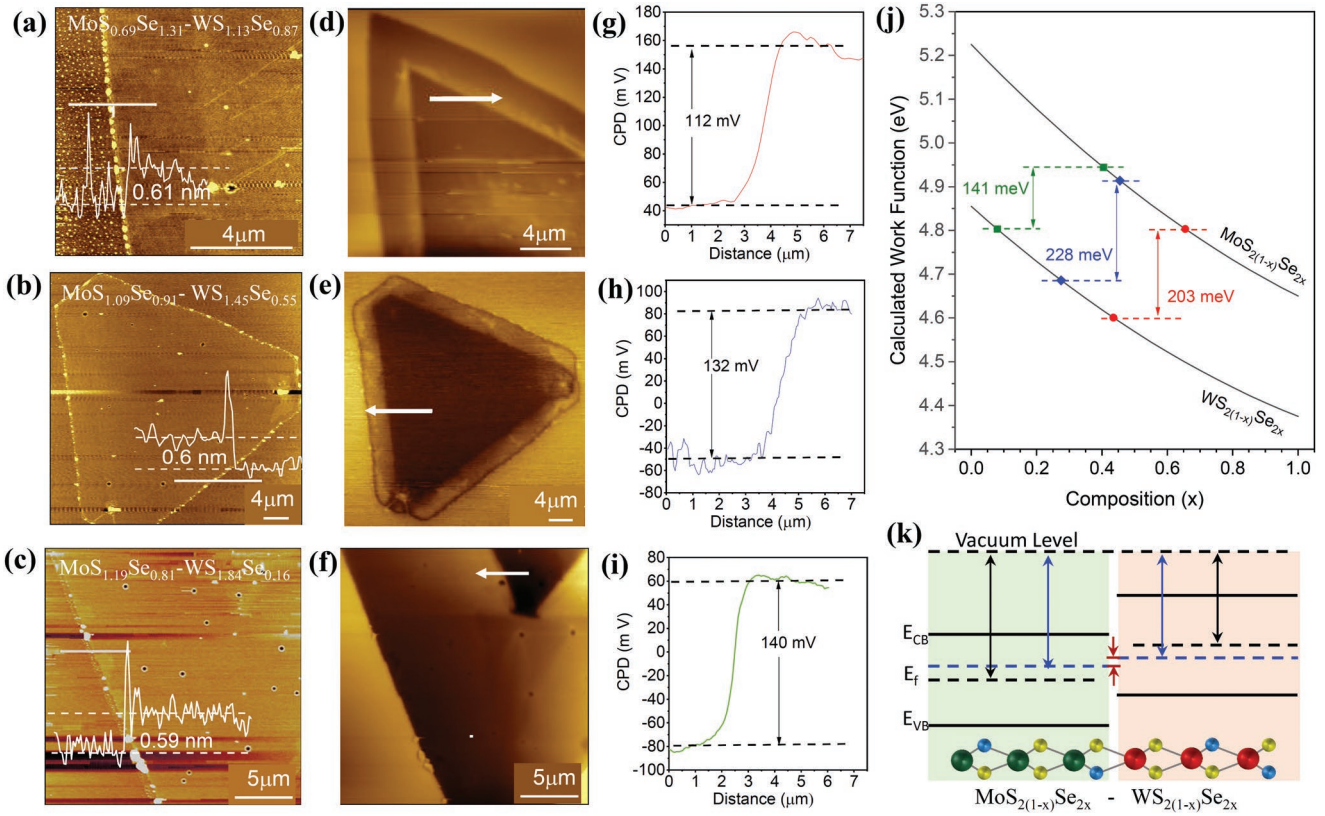

Figure 5. a–c) AFM images of as grown $MoSe_{2(1-x)}S_{2x}$–$WSe_{2(1-x)}S_{2x}$ heterostructures with different *x* compositions; insets are the corresponding height profiles. d–f) KPFM images and g–i) profile of the contact potential difference at the heterojunctions corresponding to the samples in panels (a)–(c), respectively. j) Composition-dependent work function calculated assuming undoped samples with the Fermi label at mid bandgap and using the bowing parameters for the conduction and valence bands, reported in ref. [45]; the values for the binary compounds were taken from ref. [34]. The red, blue, and green data points indicate the work function difference expected for the compositions in panels (a)–(c). k) Schematics showing the change in work function differences (red arrows) due to electronic doping (dashed blue lines for E_f) compared to undoped samples (dashed black line for E_f).

WSe_2-like peaks in the selenium-rich alloys (Figure 4g) present higher intensity compared to those in the sulfur-rich alloy (Figure 3f). Also for this composition, a Raman line scan across the domains (Figure S1d,e, Supporting Information) shows no intradomain variations of the relative peak intensities and position, suggesting a homogeneous composition across each individual domain.

2.2. Composition-Dependent Band Alignment

KPFM provides the spatial distribution of the contact potential difference (CPD) between the conductive tip and the surface of the analyzed material, which can be correlated to the work function of the materials. The versatility of KPFM to study grain boundaries, edge effects, oxidation/aging, doping, and spatial distribution of intrinsic defects in TMDs has previously been demonstrated.[39,40] Although the absolute values of work functions obtained by in-air KPFM measurements are affected by surface adsorbates,[41] this technique has been used to quantify the relative change in work function across 2D heterojunctions[27,42,43] and width of the depletion region.[43,44] We mapped the CPD in three representative samples with 1L-LHSs having different combinations of chalcogen compositions in each domain (**Figure 5**). The atomic force microscopy (AFM) topography images (Figure 5a–c) and height profiles (insets) indicate a thickness of ≈0.6 nm, which is consistent with monolayers. Their corresponding KPFM images and CPD profiles are shown in Figure 5d–i. A simple inspection of the CPD profiles (Figure 5g–i) might suggest that decreasing the selenium content increases the work function difference across the heterojunction. However, this analysis must take into consideration that, for each heterostructure considered here, the chalcogen content in both domains is not the same, and differences in electronic doping due to, for instance, chalcogen vacancies, surface absorbates, or trapped charges at the SiO_2 surface can further affect this scenario.

For comparison purposes, in Figure 5j, we plot the composition-dependent work function, expected from theory[34,45] for both ternary domains ($MoS_{2(1-x)}Se_{2x}$ and $WS_{2(1-x)}Se_{2x}$) assuming undoped samples (Fermi level at mid bandgap). For this calculation, we used the values of the valence and conduction band energies for the binary compounds reported by Kim and Choi[45] using the GW method, and the Vegard's law with band bowing parameters reported by Kang et al.[34] Highlighted with different colors (green, blue, and red) are the expected work function differences according to their chalcogen compositions for the three heterostructures considered in Figure 5g–i. As

we can see, the values for the CPD change across the junction, obtained experimentally (144, 132, and 112 meV) differ from the expected values for undoped samples (141, 228, and 203 meV). Only the heterostructure with a lower selenium content (green) shows a good agreement between experiment and theory. This discrepancy between the expected and measured work function differences across the heterojunctions is very common in the literature[27,44] because TMDs and other 2D materials are unintentionally doped during the synthesis. The unintentional doping changes the position of the Fermi level and hence the difference in work functions measured experimentally. The band diagram in Figure 5k schematically shows the differences in relative position of the Fermi levels for undoped (dashed black lines) and doped (dashed blue line) samples. The shallower CPD profiles across the junctions, obtained experimentally, are also in agreement with our previous report[17] where the Mo-rich and W-rich domains grown by this method were found to be n- and p-type doping, respectively.

2.3. 2L-LHS Based on Ternary Alloys

2L-LHSs and 3L-LHSs based on ternary alloys were also observed in our samples, but in less quantities. **Figure 6**a shows an optical image of a bilayer heterostructure with the composition of $MoS_{1.47}Se_{0.53}$–$WS_{1.64}Se_{0.36}$; the thickness was corroborated by AFM (Figure 6b). The ternary nature of the 2L-LHSs was also verified by EDS elemental analysis and atomic resolution STEM (Figure S4, Supporting Information). The Raman intensity maps (Figure 6c–f) confirm the spatial distribution of the Mo and W in the core and shell domains, respectively. A Raman line profile across the heterojunction, in the growth direction (white arrow), is shown in Figure 6g. It is noticeable that the Raman peaks on each domain remain relatively constant in wavenumber along the line scan, suggesting a good homogeneity in composition. For the molybdenum-rich domain, the strongest Raman peaks are at 273 cm^{-1} ($MoSe_2$-like A_{1g}), 375 cm^{-1} (MoS_2-like E_{2g}), and 407 cm^{-1} (MoS_2-like A_{1g}). In contrast, the tungsten-rich domain presents the most relevant peaks at 165 cm^{-1} (LA), 263 cm^{-1} (WSe_2-like A_{1g}), 330 cm^{-1} (2LA), 353 cm^{-1} (WS_2-like E_{2g}), and 413 cm^{-1} (WS_2-like A_{1g}).

The PL line scan in Figure 6h also confirms a relatively homogeneous composition in each domain of the LHS, since their corresponding PL peaks remain at constant energy positions. The bilayer Mo-rich domain exhibits PL peaks at 1.73 eV (exciton A) and 1.90 eV (exciton B), while the W-rich domain only has a peak at 1.84 eV corresponding to exciton A. For bilayers, $MoSe_2$ excitons A and B can be observed with similar intensities due to a reduction in exciton A intensity, since the material is no longer a direct bandgap semiconductor like the monolayer case. The energy difference between excitons A and B, due to spin–orbit (SO) splitting of the valence band, measured in our sample is around 170 meV, which is within the values of 150 and 220 meV, previously reported for 2L MoS_2 and $MoSe_2$, respectively.[46]

2.4. Alloy-Based 3L-LHS

In this section, we examine a 3L-LHS with four domains (three junctions). **Figure 7**a shows an optical image of this alloy-based heterostructure. Although 1L, 2L, and 3L can be easily identified from optical images due to their distinct optical contrast, the thickness was further confirmed by AFM (Figure 7b). The Raman maps corresponding to the MoS_2-like, $MoSe_2$-like, WS_2-like, and WSe_2-like A_{1g} phonon modes

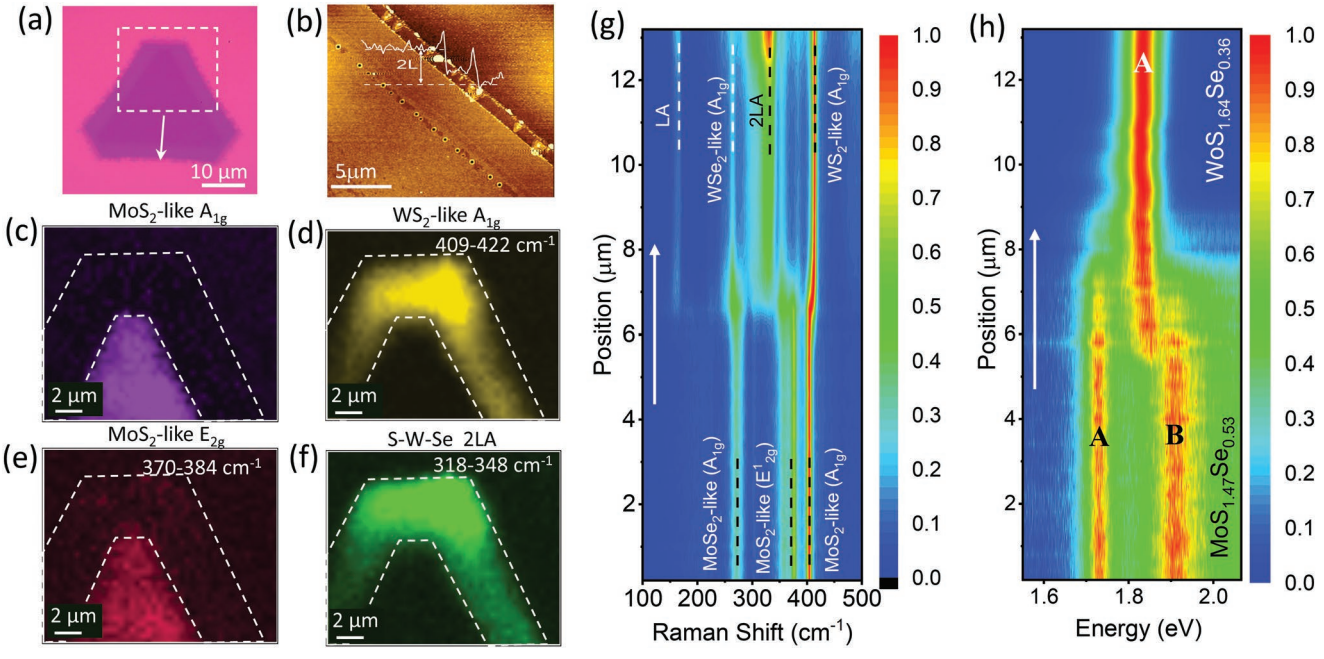

Figure 6. Bilayer (2L) lateral heterostructure $MoS_{1.47}Se_{0.53}$–$WS_{1.64}Se_{0.36}$. a) Optical image. b) AFM image and height profile. c–f) Raman maps. g,h) Raman and PL line scans, respectively. The color scales in panels (g) and (h) correspond to the normalized intensities.

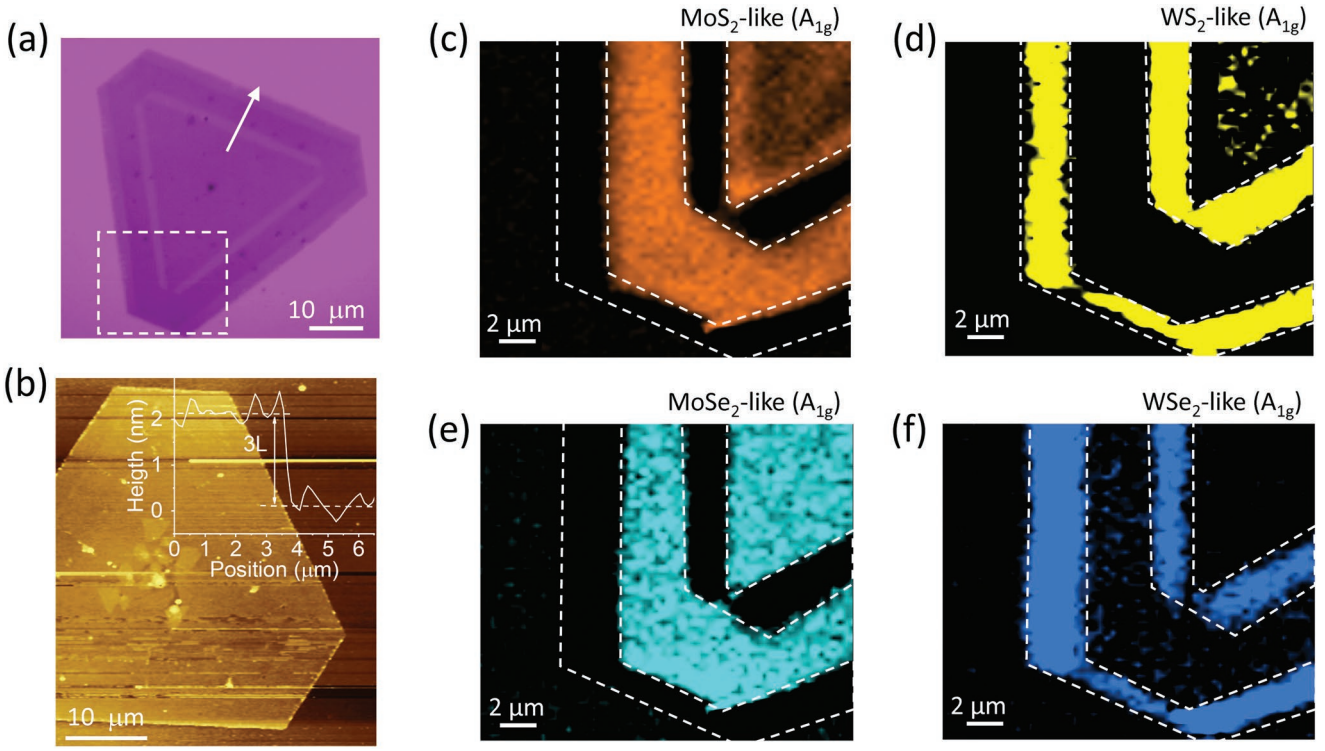

Figure 7. Trilayer (3L) lateral heterostructure $Mo_{1-\gamma}W_{\gamma}S_{2(1-x)}Se_{2x}$–$WS_{2(1-x)}Se_{2x}$ with four domains. a) Optical image. b) AFM image and height profile (inset). c–f) Raman maps corresponding to the region within the dashed square in panel (a).

(Figure 7c–f) reveal well-defined alternated domains where the MoX_2 modes are only present in the first and third domains, while the WX_2 modes are mainly confined to the second and fourth domains.

A photoluminescence line scan across the entire 3L-LHS (**Figure 8**) displays three PL features for the Mo-rich domains, which are assigned to the indirect bandgap transition (*I*) and excitons A and B, while the W-rich domain displays only a single peak corresponding to exciton A. The indirect bandgaps for few-layered WSe_2 and WS_2 have been reported to be within the range of 1.5–1.7 eV.[47] Coincidentally, the peak for exciton A has an asymmetric broadening toward lower energies precisely in the same energy range. We can tentatively assign this lower-energy tail to the indirect bandgap of the W domain. Exciton B in the W-rich domain cannot be observed with the excitation laser (523 nm) used in our experiments. Interestingly, within each individual domain, the positions of the PL peaks are approximately constant with very small variation across the domain, suggesting that even for this rare case of a multijunction 3L-LHS, the intradomain chemical composition is relatively homogeneous. However, PL peaks for the third domain (Mo rich) are slightly redshifted compared to the first Mo-rich domain. A similar redshift is observed when comparing the W-rich domains (second and fourth domains). This redshift could be the result of a change in chalcogen precursors' supply during the growth (less sulfur); sulfur is more volatile than selenium and could deplete faster over time.

As mentioned above, the energy difference between excitons A and B (ΔE_{B-A}), due to SO coupling, has typical values for MoS_2 and $MoSe_2$ between 100 and 250 meV.[46,48–50] A gradual increase of the ΔE_{B-A} for increasing W content has been reported in $Mo_{1-\gamma}W_{\gamma}Se_2$ and $Mo_{1-\gamma}W_{\gamma}S_2$ alloys.[49,50] Interestingly, the ΔE_{B-A} values obtained for the first and third domains (Figure 8a) are 244 and 330 meV, respectively. Although, ΔE_{B-A} values up to 250 meV have been reported for 3L $MoSe_2$,[46] the large values obtained for the 3L-LHS within the Mo-rich domain are an indication of a small W content. Hence, the first and third Mo-rich domains are, in fact, quaternary alloys, $Mo_{1-\gamma}W_{\gamma}S_{2(1-x)}Se_{2x}$, with a small W content ($\gamma < 0.3$ according to Wang et al.[49]). The incorporation of W to the heterostructure during the Mo-steps can be achieved by slightly reducing the amount of H_2O vapor in the carrier gas, which also reduces the concentration of tungsten hydroxides and allows small amounts of tungsten oxides species to be formed. In contrast to the hydroxides, which are volatile at the growth temperature,[16,17] the oxide species can deposit on the substrate and incorporates in small amounts to the growing material even in the MoX_2 step.

3. Conclusion

To summarize, lateral heterostructures, composed of $MoSe_{2(1-x)}S_{2x}$–$WSe_{2(1-x)}S_{2x}$ ternary alloy domains, were successfully synthesized using the one-pot water-assisted CVD method. By only changing the ratio between the source powders, we demonstrated continuous bandgap tuning in each domain of the heterostructures. Alloy-based lateral heterostructures with 2L and 3L thicknesses with homogeneous intradomain composition were also studied. For the case of 3L-LHSs, we report the realization of multijunction

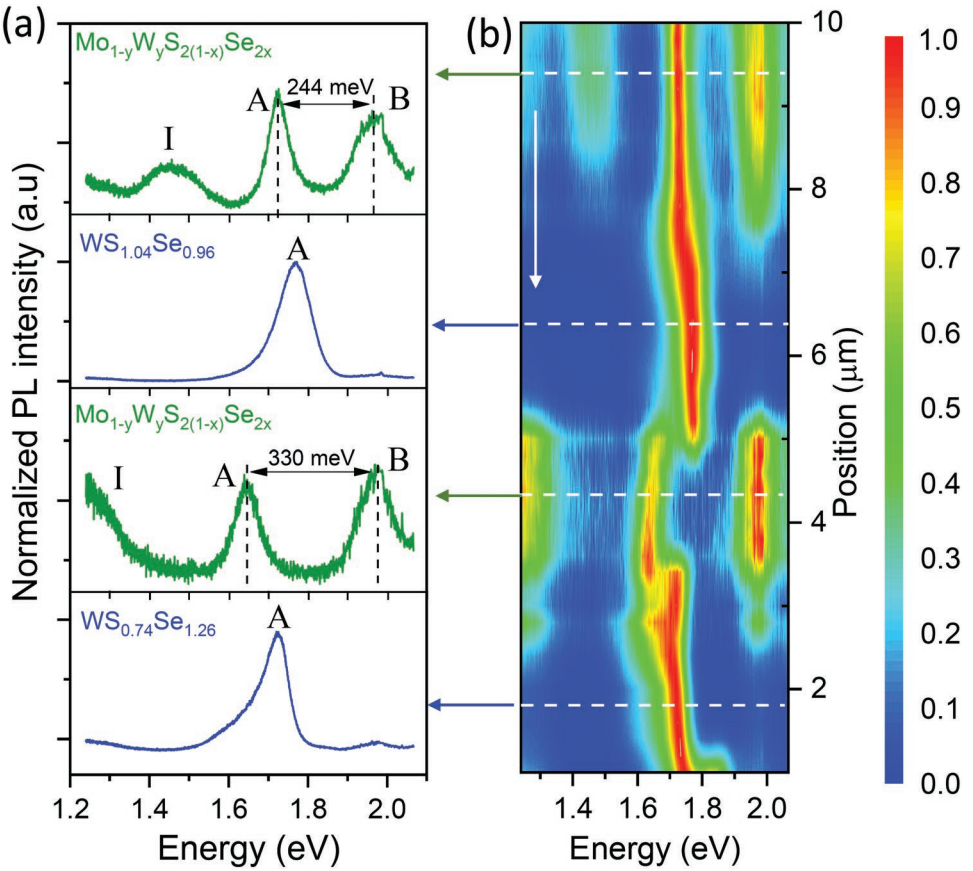

Figure 8. Trilayer (3L) lateral heterostructure $Mo_{1-y}W_yS_{2(1-x)}Se_{2x}$–$WS_{2(1-x)}Se_{2x}$ with four domains. a) Representative PL spectra for each domain. b) Color contour plot along white arrow in Figure 7a, from the inner (top) to the outer (bottom) domains.

heterostructures containing quaternary and ternary alloys, $Mo_{1-y}W_yS_{2(1-x)}Se_{2x}$–$WS_{2(1-x)}Se_{2x}$. The ability to expand the composition range and complexity in TMD-based LHSs, considerably, enhances the tools kit of 2D materials available for designing novel optoelectronic devices.

4. Experimental Section

Synthesis of Alloy-Based LHSs: LHSs were synthesized on SiO_2/Si wafers under atmospheric pressure, using the one-pot water-assisted CVD process previously developed in this group.[16,17] In short, $MoSe_2$ (99.9%, Sigma–Aldrich) and WS_2 (99.9%, Sigma–Aldrich) were used as solid precursors and placed together in a ceramic boat. In each case, both precursors were spread ½ in., so the total spread in the boat was 1 in. SiO_2/Si substrates were precleaned with acetone, isopropanol, and deionized water. During the growth, the substrates were placed downstream (700 and 750 °C), and the boat was kept at 1060 °C. N_2 gas (200 sccm) bubbled through water to favor the growth of Mo-rich domains. Subsequently, it was changed to Ar + 5% H_2 (200 sccm) to favor the growth of W-rich domains.

Raman and Photoluminescence Characterization: The Raman and photoluminescense experiments were performed by a confocal microscope Raman spectrometer (LabRAM HR Evolution, Horiba Scientific) using a backscattering geometry. The excitation wavelength of the laser was 532 nm, and the maps were done with a 100× objective (numerical aperture = 0.9, working distance = 0.21 mm). During the PL and the Raman mapping, the optical path was stationary, while moving the sample on a computer-controlled motorized *XY* stage.

Atomic Force Microscopy: AFM measurements were conducted using an OmegaScopeR atomic force microscope (Horiba Scientific). Standard AFM probes with pyramidal silicon tips and resonance frequency 265–410 kHz were used for topography AFM measurements. Pt-coated silicon tips with the resonance frequency of 60–90 kHz in noncontact mode (tapping mode) were used for Kelvin probe measurements of the surface potential.

Transmission Electron Microscopy: High-angle annular dark-field scanning transmission electron microscopy (HAADF-STEM) imaging was carried out on a probe-aberration-corrected JEOL JEM-ARM200cF with a cold-field emission gun at 200 kV. The STEM resolution of the microscope was 0.78 Å. The HAADF-STEM images were collected with the JEOL HAADF detector using the following experimental conditions: probe size = 7*c*, condenser lens aperture = 30 µm, scan speed = 32 µs pixel^{-1}, and camera length = 8 cm, which corresponded to a probe convergence angle of 21 mrad and an inner collection angle of 76 mrad. For EDS analysis, an Oxford x-Max SDD detector was used, and the probe size for the elemental mapping was less than 1 Å.

Supporting Information

Supporting Information is available from the Wiley Online Library or from the author.

Acknowledgements

H.R.G. acknowledges support by the National Science Foundation Grant DMR-1557434. TEM work was performed at the NHMFL, which

is supported by the NSF Cooperative Agreement No. DMR-1644779 and the State of Florida. P.K.S. acknowledges the Department of Science and Technology (DST), India (Project Code: DST/NM/QM/2019/6).

Conflict of Interest

The authors declare no conflict of interest.

Data Availability Statement

The data that support the findings of this study are available from the corresponding author upon reasonable request.

Keywords

2D materials, heterostructures, transition metal dichalcogenides

Received: October 28, 2021
Revised: December 20, 2021
Published online:

[1] S. Z. Butler, S. M. Hollen, L. Y. Cao, Y. Cui, J. A. Gupta, H. R. Gutierrez, T. F. Heinz, S. S. Hong, J. X. Huang, A. F. Ismach, E. Johnston-Halperin, M. Kuno, V. V. Plashnitsa, R. D. Robinson, R. S. Ruoff, S. Salahuddin, J. Shan, L. Shi, M. G. Spencer, M. Terrones, W. Windl, J. E. Goldberger, *ACS Nano* **2013**, *7*, 2898.
[2] H. R. Gutierrez, *ACS Appl. Nano Mater.* **2020**, *3*, 6134.
[3] W. Choi, N. Choudhary, G. H. Han, J. Park, D. Akinwande, Y. H. Lee, *Mater. Today* **2017**, *20*, 116.
[4] K. Khan, A. K. Tareen, M. Aslam, R. H. Wang, Y. P. Zhang, A. Mahmood, Z. B. Ouyang, H. Zhang, Z. Y. Guo, *J. Mater. Chem. C* **2020**, *8*, 387.
[5] R. T. Lv, H. Terrones, A. L. Elias, N. Perea-Lopez, H. R. Gutierrez, E. Cruz-Silva, L. P. Rajukumar, M. S. Dresselhaus, M. Terrones, *Nano Today* **2015**, *10*, 559.
[6] K. F. Mak, J. Shan, *Nat. Photonics* **2016**, *10*, 216.
[7] E. C. Ahn, *npj 2D Mater. Appl.* **2020**, *4*, 17.
[8] J. R. Schaibley, H. Y. Yu, G. Clark, P. Rivera, J. S. Ross, K. L. Seyler, W. Yao, X. D. Xu, *Nat. Rev. Mater.* **2016**, *1*, 16055.
[9] B. Kundu, P. Mohanty, P. Kumar, B. Nayak, B. Mahato, P. Ranjan, S. K. Chakraborty, S. Sahoo, P. K. Sahoo, *Emergent Mater.* **2021**, *4*, 923.
[10] X. D. Duan, C. Wang, J. C. Shaw, R. Cheng, Y. Chen, H. L. Li, X. P. Wu, Y. Tang, Q. L. Zhang, A. L. Pan, J. H. Jiang, R. Q. Yu, Y. Huang, X. F. Duan, *Nat. Nanotechnol.* **2014**, *9*, 1024.
[11] Y. J. Gong, J. H. Lin, X. L. Wang, G. Shi, S. D. Lei, Z. Lin, X. L. Zou, G. L. Ye, R. Vajtai, B. I. Yakobson, H. Terrones, M. Terrones, B. K. Tay, J. Lou, S. T. Pantelides, Z. Liu, W. Zhou, P. M. Ajayan, *Nat. Mater.* **2014**, *13*, 1135.
[12] C. M. Huang, S. F. Wu, A. M. Sanchez, J. J. P. Peters, R. Beanland, J. S. Ross, P. Rivera, W. Yao, D. H. Cobden, X. D. Xu, *Nat. Mater.* **2014**, *13*, 1096.
[13] Y. J. Gong, S. D. Lei, G. L. Ye, B. Li, Y. M. He, K. Keyshar, X. Zhang, Q. Z. Wang, J. Lou, Z. Liu, R. Vajtai, W. Zhou, P. M. Ajayan, *Nano Lett.* **2015**, *15*, 6135.
[14] Z. W. Zhang, P. Chen, X. D. Duan, K. T. Zang, J. Luo, X. F. Duan, *Science* **2017**, *357*, 788.
[15] S. E. Xie, L. J. Tu, Y. M. Han, L. J. Huang, K. Kang, K. U. Lao, P. Poddar, C. Park, D. A. Muller, R. A. DiStasio, J. Park, *Science* **2018**, *359*, 1131.
[16] P. K. Sahoo, S. Memaran, F. A. Nugera, Y. Xin, T. D. Marquez, Z. G. Lu, W. K. Zheng, N. D. Zhigadlo, D. Smirnov, L. Balicas, H. R. Gutierrez, *ACS Nano* **2019**, *13*, 12372.
[17] P. K. Sahoo, S. Memaran, Y. Xin, L. Balicas, H. R. Gutierrez, *Nature* **2018**, *553*, 63.
[18] M. Mahjouri-Samani, M. W. Lin, K. Wang, A. R. Lupini, J. Lee, L. Basile, A. Boulesbaa, C. M. Rouleau, A. A. Puretzky, I. N. Ivanov, K. Xiao, M. Yoon, D. B. Geohegan, *Nat. Commun.* **2015**, *6*, 7749.
[19] T. Afaneh, P. K. Sahoo, I. A. P. Nobrega, Y. Xin, H. R. Gutierrez, *Adv. Funct. Mater.* **2018**, *28*, 1802949.
[20] S. Tongay, D. S. Narang, J. Kang, W. Fan, C. H. Ko, A. V. Luce, K. X. Wang, J. Suh, K. D. Patel, V. M. Pathak, J. B. Li, J. Q. Wu, *Appl. Phys. Lett.* **2014**, *104*, 012101.
[21] Y. F. Chen, J. Y. Xi, D. O. Dumcenco, Z. Liu, K. Suenaga, D. Wang, Z. G. Shuai, Y. S. Huang, L. M. Xie, *ACS Nano* **2013**, *7*, 4610.
[22] J. Park, M. S. Kim, B. Park, S. H. Oh, S. Roy, J. Kim, W. Choi, *ACS Nano* **2018**, *12*, 6301.
[23] Q. L. Feng, N. N. Mao, J. X. Wu, H. Xu, C. M. Wang, J. Zhang, L. M. Xie, *ACS Nano* **2015**, *9*, 7450.
[24] X. D. Duan, C. Wang, Z. Fan, G. L. Hao, L. Z. Kou, U. Halim, H. L. Li, X. P. Wu, Y. C. Wang, J. H. Jiang, A. L. Pan, Y. Huang, R. Q. Yu, X. F. Duan, *Nano Lett.* **2016**, *16*, 264.
[25] L. M. Xie, *Nanoscale* **2015**, *7*, 18392.
[26] Q. Fu, L. Yang, W. H. Wang, A. Han, J. Huang, P. W. Du, Z. Y. Fan, J. Y. Zhang, B. Xiang, *Adv. Mater.* **2015**, *27*, 4732.
[27] B. Y. Zheng, C. Ma, D. Li, J. Y. Lan, Z. Zhang, X. X. Sun, W. H. Zheng, T. F. Yang, C. G. Zhu, G. Ouyang, G. Z. Xu, X. L. Zhu, X. Wang, A. L. Pan, *J. Am. Chem. Soc.* **2018**, *140*, 11193.
[28] H. L. Li, Q. L. Zhang, X. D. Duan, X. P. Wu, X. P. Fan, X. L. Zhu, X. J. Zhuang, W. Hu, H. Zhou, A. L. Pan, X. F. Duan, *J. Am. Chem. Soc.* **2015**, *137*, 5284.
[29] S. J. Zheng, L. F. Sun, T. T. Yin, A. M. Dubrovkin, F. C. Liu, Z. Liu, Z. X. Shen, H. J. Fan, *Appl. Phys. Lett.* **2015**, *106*, 063113.
[30] A. Azizi, Y. X. Wang, Z. Lin, K. Wang, A. L. Elias, M. Terrones, V. H. Crespi, N. Alem, *Nano Lett.* **2016**, *16*, 6982.
[31] S. Susarla, J. A. Hachtel, X. T. Yang, A. Kutana, A. Apte, Z. H. Jin, R. Vajtai, J. C. Idrobo, J. Lou, B. I. Yakobson, C. S. Tiwary, P. M. Ajayan, *Adv. Mater.* **2018**, *30*, 1804218.
[32] H. Yu, H. Yan, H. Li, Z. C. Li, Y. L. Bai, H. Zhu, S. G. Yin, *ACS Appl. Mater. Interfaces* **2021**, *13*, 44693.
[33] J. Lee, S. Pak, Y. W. Lee, Y. Park, A. R. Jang, J. Hong, Y. Cho, B. Hou, S. Lee, H. Y. Jeong, H. S. Shin, S. M. Morris, S. Cha, J. I. Sohn, J. M. Kim, *ACS Nano* **2019**, *13*, 13047.
[34] J. Kang, S. Tongay, J. B. Li, J. Q. Wu, *J. Appl. Phys.* **2013**, *113*, 143703.
[35] Q. L. Feng, Y. M. Zhu, J. H. Hong, M. Zhang, W. J. Duan, N. N. Mao, J. X. Wu, H. Xu, F. L. Dong, F. Lin, C. H. Jin, C. M. Wang, J. Zhang, L. M. Xie, *Adv. Mater.* **2014**, *26*, 2648.
[36] J. Jadczak, D. O. Dumcenco, Y. S. Huang, Y. C. Lin, K. Suenaga, P. H. Wu, H. P. Hsu, K. K. Tiong, *J. Appl. Phys.* **2014**, *116*, 193505.
[37] A. Berkdemir, H. R. Gutierrez, A. R. Botello-Mendez, N. Perea-Lopez, A. L. Elias, C. I. Chia, B. Wang, V. H. Crespi, F. Lopez-Urias, J. C. Charlier, H. Terrones, M. Terrones, *Sci. Rep.* **2013**, *3*, 1755.
[38] W. J. Zhao, Z. Ghorannevis, K. K. Amara, J. R. Pang, M. Toh, X. Zhang, C. Kloc, P. H. Tan, G. Eda, *Nanoscale* **2013**, *5*, 9677.
[39] X. Y. Wang, J. D. Dan, Z. L. Hu, J. F. Leong, Q. Zhang, Z. Y. Qin, S. S. Li, J. P. Lu, S. J. Pennycook, W. X. Sun, C. H. Sow, *Chem. Mater.* **2019**, *31*, 7970.
[40] D. Moore, K. Jo, C. Nguyen, J. Lou, C. Muratore, D. Jariwala, N. R. Glavin, *npj 2D Mater. Appl.* **2020**, *4*, 44.
[41] Y. L. Feng, K. L. Zhang, H. Li, F. Wang, B. Z. Zhou, M. X. Fang, W. C. Wang, J. Wei, H. S. P. Wong, *Nanotechnology* **2017**, *28*, 295705.
[42] M. J. Shearer, M. Y. Li, L. J. Li, S. Jin, R. J. Hamers, *J. Phys. Chem. C* **2018**, *122*, 13564.

[43] N. Zhou, R. Y. Wang, X. Zhou, H. Y. Song, X. Xiong, Y. Ding, J. T. Lu, L. Gan, T. Y. Zhai, *Small* **2018**, *14*, 1702731.
[44] M. Y. Li, Y. M. Shi, C. C. Cheng, L. S. Lu, Y. C. Lin, H. L. Tang, M. L. Tsai, C. W. Chu, K. H. Wei, J. H. He, W. H. Chang, K. Suenaga, L. J. Li, *Science* **2015**, *349*, 524.
[45] H. G. Kim, H. J. Choi, *Phys. Rev. B* **2021**, *103*, 085404.
[46] Y. Niu, S. Gonzalez-Abad, R. Frisenda, P. Marauhn, M. Druppel, P. Gant, R. Schmidt, N. S. Taghavi, D. Barcons, A. J. Molina-Mendoza, S. M. de Vasconcellos, R. Bratschitsch, D. P. De Lara, M. Rohlfing, A. Castellanos-Gomez, *Nanomaterials* **2018**, *8*, 725.
[47] W. J. Zhao, R. M. Ribeiro, M. L. Toh, A. Carvalho, C. Kloc, A. H. C. Neto, G. Eda, *Nano Lett.* **2013**, *13*, 5627.
[48] Y. Zhang, T. R. Chang, B. Zhou, Y. T. Cui, H. Yan, Z. K. Liu, F. Schmitt, J. Lee, R. Moore, Y. L. Chen, H. Lin, H. T. Jeng, S. K. Mo, Z. Hussain, A. Bansil, Z. X. Shen, *Nat. Nanotechnol.* **2014**, *9*, 111.
[49] G. Wang, C. Robert, A. Suslu, B. Chen, S. J. Yang, S. Alamdari, I. C. Gerber, T. Amand, X. Marie, S. Tongay, B. Urbaszek, *Nat. Commun.* **2015**, *6*, 10110.
[50] A. F. Rigosi, H. M. Hill, K. T. Rim, G. W. Flynn, T. F. Heinz, *Phys. Rev. B* **2016**, *94*, 075440.